Title

Growth and oxidation of graphitic crystallites in soot particles within a laminar diffusion flame

Authors and affiliation

Kazuhiro Hayashida [*], Shogo Nagaoka, Hiromi Ishitani

Department of Mechanical Engineering, Kitami Institute of Technology

165 Koen-cho, Kitami, Hokkaido 090-8507, Japan

*** Corresponding author**

Kazuhiro Hayashida

Department of Mechanical Engineering, Kitami Institute of Technology

165 Koen-cho, Kitami, Hokkaido 090-8507, Japan

Phone & Fax: +81-157-26-9206

e-mail: hayashka@mail.kitami-it.ac.jp

Abstract

The growth and oxidation behaviors of graphitic crystallites in soot particles within a laminar co-flow propane diffusion flame were investigated experimentally. Soot was sampled along the flame axis and collected on a quartz-fiber filter. The soot nanostructure, i.e., the graphitic crystallite size and the amorphous carbon content in the soot particles, was characterized by Raman spectroscopy and HRTEM. The spatial distributions of the fuel, PAHs, soot and OH measured by laser diagnostic techniques are presented to examine the effect of the flame structure on the soot nanostructure. The Raman spectra of the soot show that both the graphitic crystallite size and the amorphous carbon content in the soot particles increase during the soot growth process. In addition, the crystallite size and the amorphous carbon content simultaneously decrease during the soot oxidation process by OH. HRTEM images of soot particles support that these findings obtained from the Raman spectroscopy are reasonable. The influences of the soot formation and oxidation history within the flame on the soot nanostructure are validated.

Keywords: Diffusion flame; Soot; Nanostructure; Raman spectroscopy

1. Introduction

Soot emissions from such practical combustion devices as diesel engines, gas turbines and furnaces cause serious problems for the environment and human health. In addition, soot particles generated within combustion chambers reduce the durability of the combustion devices. Thus, an understanding of the mechanisms behind the inception, growth and oxidation of soot during combustion is crucial for the development of soot-reduction strategies. These mechanisms have been investigated extensively over many years; nevertheless, the evolution of soot during combustion processes has not yet been fully understood, not only in practical combustion environments but also in simple laboratory flames.

Soot consists of small sub-micron particles that primarily contain carbon, and its internal nanostructure with respect to amorphous carbon, graphitic crystalline size and their arrangements might be related to the soot formation and growth conditions [1]. Vander Wal and Tomasek [2] investigated the differences in soot nanostructures based on formation and growth conditions by means of thermal pyrolysis of various hydrocarbons; their results clearly showed that the nanostructure of soot does depend on the initial fuel identity and the synthesis conditions. Similarly, Shaddix et al. [3] and Alfè et al. [4] showed that the soot nanostructure was affected by its formation chemistry and temperature history in the flames. It is well known that amorphous carbon is more reactive than crystalline carbon [5], and furthermore, the oxidative reactivity of crystalline carbon differs with the size, orientation and organization of the crystallite [6,7]. Thus, the oxidative reactivity of soot varies according to the soot nanostructure.

Raman spectroscopy is one characterization tool used to investigate the nanostructure of carbonaceous materials. Recently, correlation of such Raman spectroscopic parameters as peak positions, widths, and intensity ratios with the structure of disordered carbonaceous materials have been examined in detail [8-11], and valuable information on the carbon nanostructure can be obtained by analyzing the spectral profile of Raman scattering. Raman spectroscopy has been applied to characterize the nanostructure of soot emitted from practical combustion devices, and the relationship between the soot nanostructure and its oxidation reactivity has been examined [11-14].

Although the nanostructure of soot emitted from combustion devices is considered variable in terms of soot formation, growth and oxidation history within the flame, the processes of structural change in the

soot nanostructure during combustion have not yet been fully understood. To clarify the effect of the soot growth and oxidation processes on the soot nanostructure, we examined the structural change in the soot nanostructure during combustion processes using a simple diffusion flame. The soot was sampled at different heights in the test flame, and its nanostructure was analyzed using Raman spectroscopy.

2. Experimental

2.1 Burner

The test flame used in this study was a laminar co-flow propane diffusion flame at atmospheric pressure. Propane was selected as the test fuel since propane is one of the most common gaseous fuels and its diffusion combustion yields the soot relatively dense within the flame [15,16]. The burner consisted of two concentric nozzles with inner diameters of 6 mm and 56 mm, and the fuel gas flowed through the inner nozzle. The flame length was defined as the distance from the nozzle rim to the luminous flame tip and was set to 30 mm. The fuel flow rate was set to 50 mL/min. To stabilize the flame, an annular airflow was supplied to the outer nozzle with a velocity of 0.5 m/s.

Axial velocity along the flame axis was calculated based on the buoyant acceleration of the flame gases given by Roper [17]. The acceleration due to buoyancy, a, is assumed to be constant (25 m/s^2), and the axial velocity, U_z, is given as [18]:

$$U_z = (U_{z0}^2 + 2az)^{1/2}, \quad (1)$$

where U_{z0} is flow velocity of fuel at the nozzle exit. Cumulative residence time of soot particles within the flame, τ_z, along the axial streamline was obtained from the following equation:

$$\tau_z = \int_0^z \frac{dz}{U_z}, \quad (2)$$

2.2 Soot sampling

Soot-containing combustion gas was sucked out of the flame via iso-kinetic sampling by means of a stainless-steel probe inserted vertically into the flame, and the soot was collected on a quartz-fiber filter. Santamaría et al. [19,20] confirmed that the soot particles sampled by the stainless-steel probe had the same properties with that of a quartz probe. Thus, the catalytic effects on soot properties were expected to be negligible small in the process of soot sampling. The soot sampling was performed on the flame axis

between z=16mm and 28mm. Suction rate was controlled with a needle valve and syringe system [16], and was set between 21 mL/min (distance from the nozzle z=16mm) and 27 mL/min (z=28 mm). The soot deposited on the sampling probe was periodically burnt off by another blue flame, and furthermore, soot residue in the probe inner wall after the sampling was removed before each measurement. The probe with an outer diameter of 1.0 mm and an inner diameter of 0.7 mm caused little or no visible disturbance. However, this inner diameter might be somewhat large with respect to the luminous flame width near the flame tip (~ 2.2 mm). Therefore, soot particles sampled near the flame tip might partially include soot formed around the flame axis.

2.3 Soot characterization

The soot nanostructure was characterized using Raman spectroscopy. Figure 1 shows a schematic of the Raman spectroscopy system. This system consisted of an Ar^+ laser (NEC, GLG3202) and a spectrograph (Horiba Jobin Yvon, iHR320) fitted with a CCD camera (Hamamatsu photonics, C704). A laser wavelength of 488 nm was applied for the Raman spectroscopy, and a laser line filter was used to attenuate the background plasma line contained in the laser light. To avoid modification of the soot nanostructure due to laser-induced heating effects [21], a defocused laser beam was applied to the soot sample on the quartz-fiber filter. Scattered light from the sample was collected in the backscattering configuration with an incident beam perpendicular to the sample surface. The Raman spectrum was captured by the CCD camera through the spectrograph. The grating of the spectrograph contained 1200 grooves/mm, and the entrance slit of the spectrograph was set at 700 μm, producing a spectral resolution of 1.6 nm. A notch filter was placed in front of the spectrograph to eliminate the Mie scattering component.

Morphology of soot particles was evaluated by means of high-resolution transmission electron microscopy (HRTEM). Soot samples on the quartz-fiber filter were ultrasonically dispersed in ethanol, and then a droplet of the colloidal solution was placed on a lacey carbon film coated TEM grid. The grid and sample was dried in the atmosphere. Soot particles were observed by a field-emission transmission electron microscope (JEOL, JEM-2010F) operated at 200 kV with point resolution of 0.19 nm.

2.4 Spectral analysis of soot via Raman spectroscopy

Figure 2 shows a typical Raman spectrum of soot. Soot was sampled at a distance from the nozzle z=16 mm in the test flame on the flame axis. The spectrum exhibits two broad and strongly overlapping peaks at approximately 1340 cm^{-1} and 1590 cm^{-1} corresponding to the G and D peaks, respectively. The G peak represents the characteristic of an ideal graphitic structure, and the D peak is associated with the nature of disordered graphite. A detailed analysis of the spectrum reveals the presence of five bands [9-13], as represented in Fig. 2. The G band is attributed to the ideal graphitic lattice vibration mode (E_{2g} symmetry) [22,23]. The D band is associated with the graphitic lattice breathing mode (A_{1g} symmetry) [22,24], which is forbidden in the ideal graphitic lattice and becomes active only in the presence of disorder. The D2 band is attributed to the disorder-induced graphitic lattice vibration mode (E_{2g} symmetry) [9,24]. The D3 band originates from the amorphous sp^2-bonded forms of carbon, such as organic molecules, fragments, and functional groups [25,26]. The D4 band is observed in the spectra of poorly organized materials such as soot and char, and is assumed to be due to the mixed sp^2-sp^3 bonds [27] and/or the sp^3-rich carbon structures [28], etc.

The Raman spectra were analyzed via curve fitting for characterization of the soot nanostructure. The Raman spectra of soot obtained near soot inception region (z=16 and 18 mm) had weak continuous background. This background would be fluorescence from PAHs associated with soot particles [29]. Thus, the background component was subtracted from obtained spectra before the spectral analysis. The spectra were processed using Carbon Analyzer FE 2011 software (Ryoka Systems Inc.) based on the least square algorithm. Sadezky et al. [9] reported that the best fitting for soot analysis consists of five bands with four Lorentzian shapes (G, D, D2 and D4) and one Gaussian shape (D3), and therefore we applied the same band combination for the curve fitting. However, there is still controversy regarding the curve fitting method. For example, Seong et al. [30] recently reported that the combination of three Lorentzian shapes (G, D and D4) and one Gaussian shape (D3) provided the most consistent results for various Raman parameters with respect to soot oxidation reactivity.

Firstly, initial values of peak position, full width at half maximum (FWHM) and intensity of each band were manually-set as optimal fit as possible, and then the least square fit was performed. The goodness-of-fit was evaluated by the reliability factor. For each Raman spectrum, the fitting procedure

was repeated six times to ensure the reproducibility of fit. The standard deviations of the reliability factor from repeated fits were typically less than 4 %. In order to confirm the repeatability of the soot sampling, sampling was performed twice at each sampling position. The Raman spectra were obtained from 3 spectra recorded at different positions of the sample.

3. Results and Discussion

3.1 Characterization of soot nanostructure

Figure 3 shows the Raman spectra of soot, which was sampled along the flame axis in the soot region, together with the curve fitting results. All spectra were normalized to the peak intensity around 1590 cm^{-1}. Although the significant change of the overall spectral profile was not confirmed, the results of the curve fitting clearly show the change of band parameters; noteworthy changes include the variations of the normalized intensities of the G and D3 bands.

Figure 4 shows the D to G peak intensity ratio (I_D/I_G) and the D3 to G peak intensity ratio (I_{D3}/I_G) on the flame axis. In addition, the axial intensity profiles of the C_3H_8-Raman, PAHs-LIF, LII and OH-LIF in the test flame (which had been clarified using laser diagnostic techniques in our previous studies [31,32]) are presented for further understanding of soot evolution within the flame. Tuinstra and Koenig [22] first reported that the I_D/I_G is inversely proportional to the in-plane graphitic crystallite size (L_a) of carbonaceous materials: $I_D/I_G \propto L_a^{-1}$. Later, Ferrari and Robertson [33] found that Tuinstra and Koenig's equation is inadequate for small crystallite and showed that in such a case the D band intensity is proportional to the area of the aromatic domains of peri-condensed hexagonal ring systems: $I_D/I_G \propto L_a^{2}$. Additionally, it has been reported that the relative intensity of the D3 band increases with the proportion of amorphous carbon content in the soot particles [13,34,35].

It can be observed that the C_3H_8-Raman rapidly decreases near the nozzle exit due to fuel pyrolysis and the rapid diffusion of molecular nitrogen to the flame axis [36]. The profile of PAHs-LIF suggests that aromatic rings are quickly formed near the nozzle exit, and its intensity increases up to near the location of fuel depletion. The peak location of PAHs-LIF coincides with the location where the LII begins to appear, and subsequently, the LII intensity increases with decreasing PAHs-LIF. This result implies that PAHs are consumed in both soot inception and soot mass growth processes [37]. In the region

of LII increase, I_D/I_G also increases. As noted previously, I_D/I_G increases with crystallite size with respect to the small crystallite (L_a<3 nm). Recent studies on soot nanostructure using high resolution transmission electron microscopy (HRTEM) [38,39] and X-ray diffraction (XRD) [13,39] have shown that the crystallite size in soot is less than 3 nm, and thus the increasing trend of I_D/I_G suggests growth of the crystallite.

The growth of the crystallite can be assumed due to a progression of thermal annealing and/or surface growth of soot particles. According to thermodynamic analysis of soot nanostructure by Hurt et al. [40], precursor nanoparticles formed from modest-sized PAHs cannot form a shell/core (onion-like) nanostructure. Therefore, it is assumed that the incipient soot particles have a disordered nanostructure. Figure 5 plots the axial flame temperature (which had been measured in our previous studies [15]) and the cumulative residence time calculated from Eq. (2) along the axial streamline based on the buoyant acceleration of the flame gases [17,18]. The temperature profile shows a dip near z=20 mm, which is an artifact resulting from soot deposition onto the thermocouple bead. Soot deposition caused an increase in the diameter of the bead, leading to changes in the temperature read by the thermocouple as the soot layer affects heat transfer properties from the flame to the bead. Since estimation of this effect is quite difficult, we didn't make the correction of temperature due to the soot deposition. Thus, the "true" temperature in the soot region must be somewhat higher than the "measured" temperature. The temperature of the crystallite growth region (z=16−22 mm) is approximately 1430 K. Vander Wal and Tomasek [2] concluded that such lower temperatures do not provide sufficient thermal activation energies for growth and reorientation of the carbon lamella in soot particles. Moreover, the residence time of the soot within the crystallite growth region is only 6 ms, and this time scale is not sufficient for thermal annealing processes [2]. Therefore, it is difficult to believe that the growth of crystallite occurred through thermal annealing. However, the crystallite growth can occur through the hydrogen-abstraction-acetylene-addition (HACA) mechanism [41] in parallel with the surface growth of the soot particle because acetylene abundantly exists within the unburned region of diffusion flames [36,42]. We speculate that our experimental results reflect the combined mechanism of HACA and the PAH condensation for the soot mass growth [37,43]. As shown in Fig. 4, increasing rate of I_D/I_G in the crystallite growth region (z=16-22 mm) is higher near the soot inception region. Since smaller crystallites in this region have more active

sites available for chemical reaction [44], this result implies that smaller crystallites grew promptly via HACA mechanism [41,43].

Similarly, the ratio of I_{D3}/I_G also increases from z=16 mm to 22 mm, which implies an increase in the amorphous carbon content in soot particles. It has been shown that the primary particle of soot is nearly spherical in shape and has a relatively ordered outer layer and a disordered core [2-6]. This disordered and amorphous core structure is often interpreted as evidence of soot nanoparticles generated by the coagulation of PAHs [45]. As noted previously, it is believed that neither the flame temperature nor the residence time within the test flame is sufficient for thermal annealing, and thus an amorphous content of primary particles could possibly remain amorphous during the soot mass growth process. It is speculated that continued addition of PAHs and other organic molecules to the external and/or interstitial surfaces of aggregated soot particles yield additional amorphous carbon, resulting in the increase of I_{D3}/I_G.

In Fig. 4, it is also worth noting that both I_D/I_G and I_{D3}/I_G decrease in the detection region of OH-LIF. This result indicates that the graphitic crystallite size and the amorphous content decrease due to the soot oxidation by OH. The OH must be the primary oxidant of soot in the test flame because the soot surface oxidation within the laminar co-flow sooting flames is dominated by OH [36,46-48]. It is well known that a carbon atom at the edge site is much more reactive than that of the basal plane carbon atom in graphitic layers; therefore, oxidation of the graphitic crystallite proceeds at the edge site and thereby reduces I_D/I_G in the OH-LIF region.

The intensity of the D2 band shown in Fig. 3 is also changed with the sampling position. The D2 band would be derived from the graphitic lattice vibration analogous to that of the G band, but becomes active in the presence of disorder. Sze et al. [49] assumed that the D2 band is originating from graphitic lattices on the external surface of carbon materials and its intensity reflects the surface area of the sample. Also, Pimenta et al. [50] reported that the edges of nanographite behave as a defect and activate the D2 band. From these reports, we speculate that the D2 band originates from the crystallite on surface layer of soot particle, and its intensity reflects disordered degree of soot surface layer and/or particle size of soot.

Figure 6 shows the HRTEM images of soot particles sampled at z=16, 20 and 26 mm together with low magnification TEM images. The TEM images show that the size of primary particles increase from z=16 mm to 20 mm due to the soot growth process and then decrease due to the oxidation by OH. The

HRTEM image at z=16 mm reveals that a soot particle has some disordered parts inside the particle. This nanostructure suggests that incipient soot particle is formed by coagulation of PAHs and primary particle is subsequently formed by coalescence of the incipient particles. The disordered parts remain in the particles of z=20 mm because thermal annealing should not be the main process of the growth of the crystallite. Outer layer of the particle (z=20 mm) is relatively ordered than that of z=16 mm, resulting from the growth of the crystallite via HACA mechanism. The HRTEM image of z=26 mm demonstrates that the oxidation of graphitic crystallite and amorphous carbon proceeded simultaneously from the outer edge of the particles.

3.2 Graphitic crystallite size of soot

The in-plane graphitic crystallite size L_a was calculated from the I_D/I_G indicated in Fig. 4 (I_D and I_G were obtained by the curve fitting) using the following equations, which are applicable for small crystallite (L_a<2−3 nm). The first equation is based on the theoretical work performed by Ferrari and Robertson [33], and the equation is given by Zickler et al. [51]:

$$\frac{I_D}{I_G} = \frac{C(\lambda_L)}{8} L_a^2 , \quad (3)$$

where $C(\lambda_L)$ is the wavelength-dependent pre-factor and λ_L is the wavelength of the laser light. Matthews et al. [52] considered the wavelength dependency of $C(\lambda_L)$ and presented the following relationship:

$$C(\lambda_L) \approx C_0 + C_1 \lambda_L , \quad (4)$$

where C_0=−12.6 nm and C_1=0.033. The $C(\lambda_L)$ value was calculated using Eq. (4), which is reported as valid for 400 nm < λ_L < 700 nm.

Another equation is based on experimental analysis performed by Lucchese et al. [53] and Cancado et al. [54]. These researchers produced single-layer graphene samples with increasing defect density by mechanical exfoliation followed by Ar^+-bombardment and obtained a phenomenological relationship between the Raman signature and defect density as follows:

$$\frac{I_D}{I_G} = C_A \frac{(r_A^2 - r_S^2)}{(r_A^2 - 2r_S^2)} \left[\exp\left(-\frac{\pi r_S^2}{L_a^2}\right) - \exp\left(-\frac{\pi (r_A^2 - r_S^2)}{L_a^2}\right) \right], \quad (5)$$

where r_A and r_S are length scales that determine the region where the D band scattering takes place and are reported as 3.1 nm and 1.0 nm, respectively. The parameter C_A corresponds to the maximum possible

I_D/I_G and is given by:

$$C_A = \frac{160}{E_L^4}, \quad (6)$$

where E_L is the excitation energy, and E_L=2.54 eV (λ_L=488 nm) is used in this study.

Table 1 lists the values of L_a derived from Eqs. (3) and (5). The L_a of Eq. (3) ranges from 1.606 nm to 2.173 nm, whereas the L_a of Eq. (5), which ranges from 1.527 nm to 2.060 nm, is slightly smaller than that of Eq. (3). Because Eq. (5) is proposed based on the experimental evidence, the latter might be closer to the true value. Similar to this study, Herdman et al. [55] estimated the crystallite size of soot sampled from within a nitrogen-diluted non-premixed ethylene/air flame using the Raman spectroscopy. Estimated crystallite size L_a ranged from 1.0 nm to 1.2 nm, and this size is somewhat smaller than our soot. This discrepancy might be arising from a fuel dilution effect and/or a difference of fuel molecule. Alternatively, the measurement region of their study was limited to comparatively low level soot region. Therefore, soot in a high soot volume fraction region might have possessed a larger crystallite equivalent to that of our soot. In contrast to the soot within flames, Chen and Dobbins [56] estimated the crystallite size of soot emitted from an ethylene diffusion flame. XRD was used to estimate the L_a, and the estimated value of L_a=2.496 nm is somewhat larger than our soot. Although the fuel molecule and flame configuration of our test flame is different from these previous works, our estimated value of graphitic crystallite size is believed to be adequate.

The size of one aromatic ring is approximately 0.25 nm, and therefore L_a=1.527 nm (z=16 mm) is equivalent to the size of six aromatic rings measured across. In our previous work, we estimated that the molecular size of PAHs near the soot inception region (z=14 mm) was near 250 amu [15], and the major soot precursors of this size contain 3−4 aromatic rings across. It is likely that soot inception (around z=14 mm) and subsequent soot growth formed the soot particles with a crystallite size of L_a=1.527 nm at z=16 mm.

Table 1

In-plane graphitic crystallite size of soot calculated from I_D/I_G.

z (mm)	I_D / I_G	L_a (nm) [Eq. (3)]	L_a (nm) [Eq. (5)]
16	1.130 ± 0.045	1.606 ± 0.032	1.527 ± 0.022
18	1.565 ± 0.006	1.890 ± 0.003	1.754 ± 0.003
20	1.883 ± 0.079	2.073 ± 0.044	1.939 ± 0.049
22	2.067 ± 0.070	2.173 ± 0.037	2.060 ± 0.049
24	1.930 ± 0.058	2.099 ± 0.032	1.969 ± 0.037
26	1.670 ± 0.016	1.953 ± 0.009	1.812 ± 0.009
28	1.380 ± 0.014	1.775 ± 0.009	1.654 ± 0.007

4. Conclusions

The growth and oxidation of graphitic crystallites in soot particles within a laminar propane diffusion flame along the flame axis were investigated experimentally. Soot was sampled at various heights in the flame on the flame axis, and its nanostructure was analyzed using Raman spectroscopy. The obtained Raman spectra were decomposed into five bands (G, D, D2, D3 and D4) via curve fitting, and the graphitic crystallite size and the amorphous carbon content in the soot particles were evaluated from the D to G peak intensity ratio (I_D/I_G) and the D3 to G peak intensity ratio (I_{D3}/I_G), respectively. Additionally, to clarify the structure of the test flame, the axial distributions of fuel (C_3H_8-Raman), PAHs-LIF, LII and OH-LIF were also indicated.

Considering the temperature and the size of PAHs around the soot inception region (previously estimated in [15]), it is presumed that the incipient soot particles had a disordered nanostructure. Subsequently growth of the graphitic crystallite was confirmed in parallel with increasing the soot concentration. In terms of the flame temperature and the residence time along the flame axis, this crystallite growth could occur through the HACA mechanism rather than the thermal annealing. Since the smaller crystallites have more active sites available for chemical reaction, comparatively prompt growth of the crystallite near the soot inception region may suggest the growth proceeded via HACA mechanism. In parallel with the crystallite growth, increase of the amorphous carbon content in the soot particles was confirmed. It is speculated that continued addition of PAHs and other organic molecules to the external and/or interstitial surfaces of aggregated soot particles yield additional amorphous carbon. When the soot particles entered into the OH region, soot underwent oxidation and therefore both the graphitic crystallite size and the amorphous carbon content decreased simultaneously. The graphitic crystallite size within the test flame was estimated to as ≈1.5−2.2 nm.

Acknowledgements

We thank Mr. Tomohiro Nomura (Marutama Industry Co., Ltd., Japan) for his experimental support. We are also grateful to Associate professor Norihito Sakaguchi and Dr. Yutaka Yoshida of Hokkaido University for their help in obtaining HRTEM images. This work was supported by JSPS KAKENHI, Grant-in-Aid for Young Scientists (B), 22760141, 2010. A part of this work was conducted at Hokkaido University, supported by "Nanotechnology Platform" Program of the Ministry of Education, Culture, Sports, Science and Technology (MEXT), Japan.

References

[1] Vander Wal RL, Strzelec A, Toops TJ, Daw CS, Genzale CL. Forensics of soot: C5-related nanostructure as a diagnostic of in-cylinder chemistry. Fuel 2013;113:522-526.

[2] Vander Wal RL, Tomasek AJ. Soot nanostructure: dependence upon synthesis conditions. Combust Flame 2004;136:129-140.

[3] Shaddix CR, Palotás ÁB, Megaridis CM, Choi MY, Yang NYC. Soot graphitic order in laminar diffusion flames and a large-scale JP-8 pool fire. Int J Heat Mass Transfer 2005;48:3604-3614.

[4] Alfè M, Apicella B, Rouzaud J-N, Tregrossi A, Ciajolo A. The effect of temperature on soot properties in premixed methane flames. Combust Flame 2010;157:1959-1965.

[5] Song J, Alam M, Boehman AL, Kim U. Examination of the oxidation behavior of biodiesel soot. Combust Flame 2006;146:589-604.

[6] Vander Wal RL, Tomasek AJ. Soot oxidation: dependence upon initial nanostructure. Combust Flame 2003;134:1-9.

[7] Ishiguro T, Suzuki N, Fujitani Y, Morimoto H. Microstructural changes of diesel soot during oxidation. Combust Flame 1991;85:1-6.

[8] Beyssac O, Goffé B, Petitet J-P, Froigneux E, Moreau M, Rouzaud J-N. On the characterization of disordered and heterogeneous carbonaceous materials by Raman spectroscopy. Spectrochim Acta Part A 2003;59:2267-2276.

[9] Sadezky A, Muckenhuber H, Grothe H, Niessner R, Pöschl U. Raman microspectroscopy of soot and related carbonaceous materials: Spectral analysis and structural information. Carbon

2005;43:1731-1742.

[10] Sheng C. Char structure characterised by Raman spectroscopy and its correlations with combustion reactivity. Fuel 2007;86:2316-2324.

[11] Knauer M, Carrara M, Rothe D, Niessner R, Ivleva NP. Changes in structure and reactivity of soot during oxidation and gasification by oxygen, studied by micro-Raman spectroscopy and temperature programmed oxidation. Aerosol Sci Technol 2009;43:1-8.

[12] Ivleva NP, Messerer A, Yang X, Niessner R, Pöschl U. Raman microspectroscopic analysis of changes in the chemical structure and reactivity of soot in a diesel exhaust aftertreatment model system. Environ Sci Technol 2007;41:3702-3707.

[13] Al-Qurashi K, Boehman AL. Impact of exhaust gas recirculation (EGR) on the oxidative reactivity of diesel engine soot. Combust Flame 2008;155:675-695.

[14] Lapuerta M, Oliva F, Agudelo JR, Boehman AL. Effect of fuel on the soot nanostructure and consequences on loading and regeneration of diesel particulate filters. Combust Flame 2012;159:844-853.

[15] Hayashida K, Mogi M, Amagai K, Arai M. Growth characteristics of polycyclic aromatic hydrocarbons in dimethyl ether diffusion flame. Fuel 2011;90:493-498.

[16] Furuhata T, Kobayashi Y, Hayashida K, Arai M. Behavior of PAHs and PM in a diffusion flame of paraffin fuels. Fuel 2012;91:16-25.

[17] Roper FG. The prediction of laminar jet diffusion flame sizes: Part I. Theoretical model. Combust Flame 1977;29:219-226.

[18] Oh KC, Shin HD. The effect of oxygen and carbon dioxide concentration on soot formation in non-premixed flames. Fuel 2006;85:615-624.

[19] Santamaría A, Mondragón F, Molina A, Marsh ND, Eddings EG, Sarofim AF. FT-IR and ^{1}H NMR characterization of the products of an ethylene inverse diffusion flame. Combust flame 2006;146:52-62.

[20] Velásquez M, Mondragón F, Santamaría A. Chemical characterization of soot precursors and soot particles produced in hexane and diesel surrogates using an inverse diffusion flame burner. Fuel 2013;104:681-690.

[21] Hu L, Wang S, Zhang B, Zeng Y. Structural changes in soot particles induced by diode laser irradiation. Carbon 2006;44:1725-1729.

[22] Tuinstra F, Koenig JL. Raman spectrum of graphite. J Chem Phys 1970;53:1126-1130.

[23] Nemanich RJ, Solin SA. First- and second-order Raman scattering from finite-size crystals of graphite. Phys Rev B 1979;20:392-401.

[24] Escribano R, Sloan JJ, Siddique N, Sze N, Dudev T. Raman spectroscopy of carbon-containing particles. Vib Spectrosc 2001;26:179-186.

[25] Cuesta A, Dhamelincourt P, Laureyns J, Martínez-Alonso A, Tascón JMD. Raman microprobe studies on carbon materials. Carbon 1994;32:1523-1532.

[26] Jawhari T, Roid A, Casado J. Raman spectroscopic characterization of some commercially available carbon black materials. Carbon 1995;33:1561-1565.

[27] Bacsa WS, Lannin JS, Pappas DL, Cuomo JJ. Raman scattering of laser-deposited amorphous carbon. Phys Rev B 1993;47:10931-10934.

[28] Schwan J, Ulrich S, Batori V, Ehrhardt H, Silva SRP. Raman spectroscopy on amorphous carbon films. J Appl Phys 1996;80:440-447.

[29] Brunetto R, Pino T, Dartois E, Cao A-T, d'Hendecourt L, Strazzulla G, Bréchignac Ph. Comparison of the Raman spectra of ion irradiated soot and collected extraterrestrial carbon, Icarus 2009;200:323-337.

[30] Seong HJ, Boehman AL. Evaluation of Raman parameters using visible Raman microscopy for soot oxidative reactivity. Energy Fuels 2013;27:1613-1624.

[31] Hayashida K, Amagai K, Satoh K, Arai M. Measurement of fuel concentration distribution in a sooting flame through Raman scattering. JSME Int J Ser B 2006;49:512-519.

[32] Hayashida K, Amagai K, Satoh K, Arai M. Experimental analysis of soot formation in sooting diffusion flame by laser-induced emissions. J Eng Gas Turbines Power-Trans ASME 2006;128:241-246.

[33] Ferrari AC, Robertson J. Interpretation of Raman spectra of disordered and amorphous carbon. Phys Rev B 2000;61:14095-14107.

[34] Ivleva NP, McKeon U, Niessner R, Pöschl U. Raman microspectroscopic analysis of size-resolved

atmospheric aerosol particle samples collected with an ELPI: soot, humic-like substances, and inorganic compounds. Aerosol Sci Technol 2007;41:655-671.

[35] Knauer M, Schuster ME, Su D, Schlögl R, Niessner R, Ivleva NP. Soot structure and reactivity analysis by Raman microspectroscopy, temperature-programmed oxidation, and high-resolution transmission electron microscopy. J Phys Chem A 2009;113:13871-13880.

[36] Smooke MD, McEnally CS, Pfefferle LD, Hall RJ, Colket MB. Computational and experimental study of soot formation in a coflow, laminar diffusion flame. Combust Flame 1999;117:117-139.

[37] Hwang JY, Chung SH. Growth of soot particles in counterflow diffusion flames of ethylene. Combust Flame 2001;125:752-762.

[38] Merchan-Merchan W, Sanmiguel SG, McCollam S. Analysis of soot particles derived from biodiesels and diesel fuel air-flames. Fuel 2012;102:525-535.

[39] Yehliu K, Vander Wal RL, Armas O, Boehman AL. Impact of fuel formulation on the nanostructure and reactivity of diesel soot. Combust Flame 2012;159:3597-3606.

[40] Hurt RH, Crawford GP, Shim H-S. Equilibrium nanostructure of primary soot particles. Proc Combust Inst 2000;28:2539-2546.

[41] Frenklach M. On surface growth mechanism of soot particles. Proc Combust Inst 1996;26:2285-2293.

[42] Onischuk AA, di Stasio S, Karasev VV, Baklanov AM, Makhov GA, Vlasenko AL, Sadykova AR, Shipovalov AV, Panfilov VN. Evolution of structure and charge of soot aggregates during and after formation in a propane/air diffusion flame. J Aerosol Sci 2003;34:383-403.

[43] Dworkin SB, Zhang Q, Thomson MJ, Slavinskaya NA, Riedel U. Application of an enhanced PAH growth model to soot formation in a laminar coflow ethylene/air diffusion flame. Combust Flame 2011;158:1682-1695.

[44] Raj A, Celnik M, Shirley R, Sander M, Patterson R, West R, Kraft M. Application of an enhanced PAH growth model to soot formation in a laminar coflow ethylene/air diffusion flame. Combust Flame 2009;156:896-913.

[45] Vander Wal RL, Yezerets A, Currier NW, Kim DH, Wang CM. HRTEM Study of diesel soot collected from diesel particulate filters. Carbon 2007;45:70-77.

[46] Puri R, Santoro RJ, Smyth KC. The oxidation of soot and carbon monoxide in hydrocarbon diffusion flames. Combust Flame 1994;97:125-144.

[47] Xu F, El-Leathy AM, Kim CH, Faeth GM. Soot surface oxidation in hydrocarbon/air diffusion flames at atmospheric pressure. Combust Flame 2003;132:43-57.

[48] de Andrade Oliveira MH, Olofsson N-E, Johnsson J, Bladh H, Lantz A, Li B, Li ZS, Aldén M, Bengtsson P-E, Luijten CCM, de Goey LPH. Soot, PAH and OH measurements in vaporized liquid fuel flames. Fuel 2013;112:145-152.

[49] Sze S-K, Siddique N, Sloan JJ, Escribano R. Raman spectroscopic characterization of carbonaceous aerosols. Atmos Environ 2001;35:561-568.

[50] Pimenta MA, Dresselhaus Gm Dresselhaus MS, Cancado LG, Jorio A, Saito R. Phys Chem Chem Phys 2007;9:1276-1291.

[51] Zickler GA, Smarsly B, Gierlinger N, Peterlik H, Paris O. A reconsideration of the relationship between the crystallite size La of carbons determined by X-ray diffraction and Raman spectroscopy. Carbon 2006;44:3239-3246.

[52] Matthews MJ, Pimenta MA. Origin of dispersive effects of the Raman D band in carbon materials. Phys Rev B 1999;59:R6585-R6588.

[53] Lucchese MM, Stavale F, Martins Ferreira EH, Vilani C, Moutinho MVO, Capaz RB, Achete CA, Jorio A. Quantifying ion-induced defects and Raman relaxation length in graphene. Carbon 2010;48:1592-1597.

[54] Cancado LG, Jorio A, Martins Ferreira EH, Stavale F, Achete CA, Capaz RB, Moutinho MVO, Lombardo A, Kulmala TS, Ferrari AC. Quantifying defects in graphene via Raman spectroscopy at different excitation energies. Nano Lett 2011;11:3190-3196.

[55] Herdman JD, Connelly BC, Smooke MD, Long MB, Miller JH. A comparison of Raman signatures and laser-induced incandescence with direct numerical simulation of soot growth in non-premixed ethylene/air flames. Carbon 2011;49:5298-5311.

[56] Chen HX, Dobbins RA. Crystallogenesis of particles formed in hydrocarbon combustion. Combust Sci Technol 2000;159:109-128.

Figure captions

Fig. 1. Schematic illustration of the Raman spectroscopy system.

Fig. 2. Typical Raman spectra of soot, and curve fitting with the five-band combination.

Fig. 3. Raman spectra of soot sampled along the flame axis.

Fig. 4. Variations of I_D/I_G and I_{D3}/I_G (top); and axial distributions of C_3H_8-Raman, PAHs-LIF, LII and OH-LIF (bottom). Axial distributions are from [31,32].

Fig. 5. Temperature and residence time profiles along the flame axis. Temperature is from [15].

Fig. 6. TEM and HRTEM images of soot particles sampled on the flame axis (z=16, 20 and 26 mm).

Figure 1

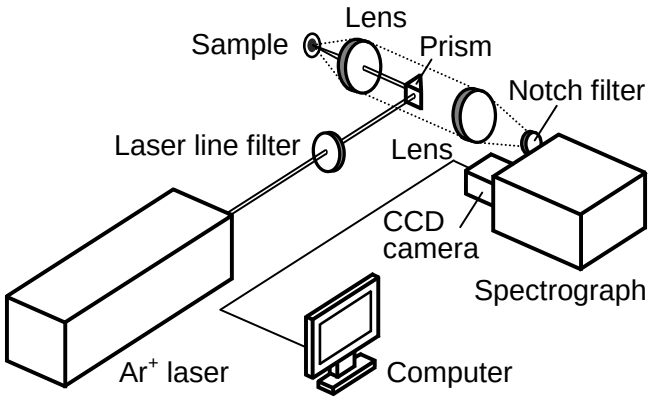
Lens
Sample
Prism
Notch filter
Laser line filter
Lens
CCD
camera
Spectrograph
Ar+ laser
Computer

Figure 2

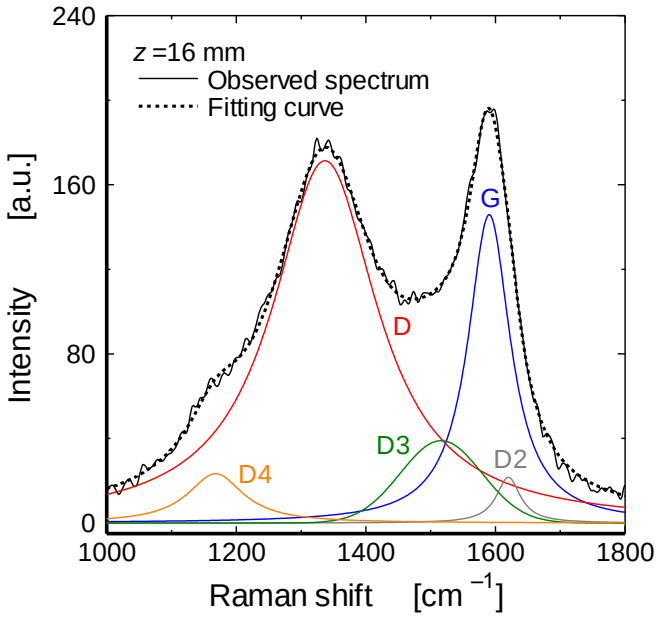
z =16 mm
Observed spectrum
Fitting curve
Intensity [a.u.]
240
160
80
0
1000
1200
1400
1600
1800
Raman shift [cm −1]
G
D
D3
D2
D4

Figure 3

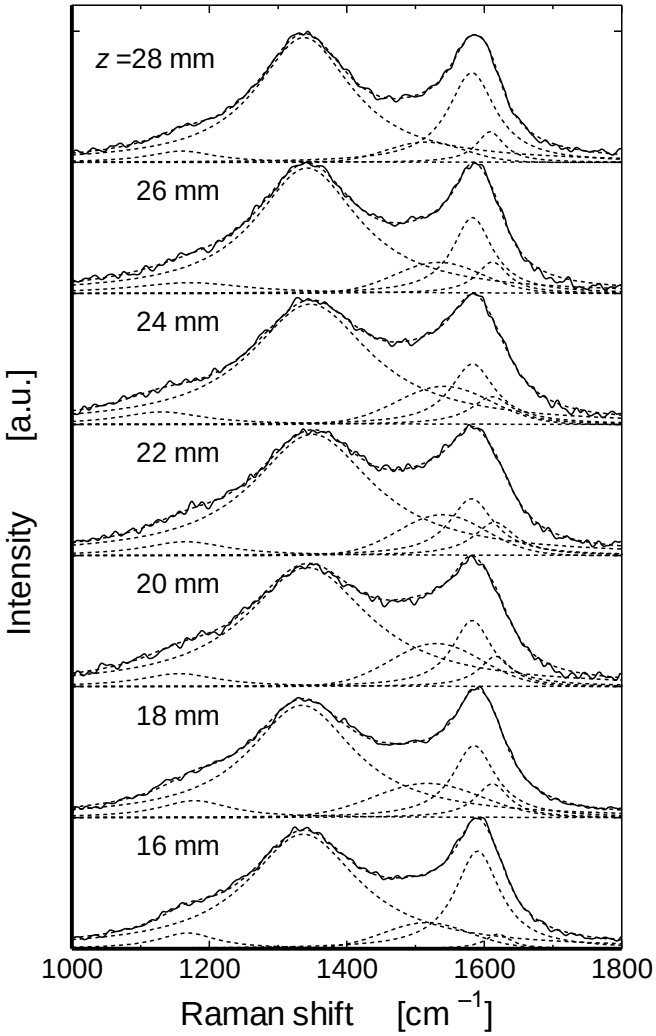
z =28 mm
26 mm
24 mm
22 mm
20 mm
18 mm
16 mm
Intensity [a.u.]
1000
1200
1400
1600
1800
Raman shift [cm −1]

Figure 4

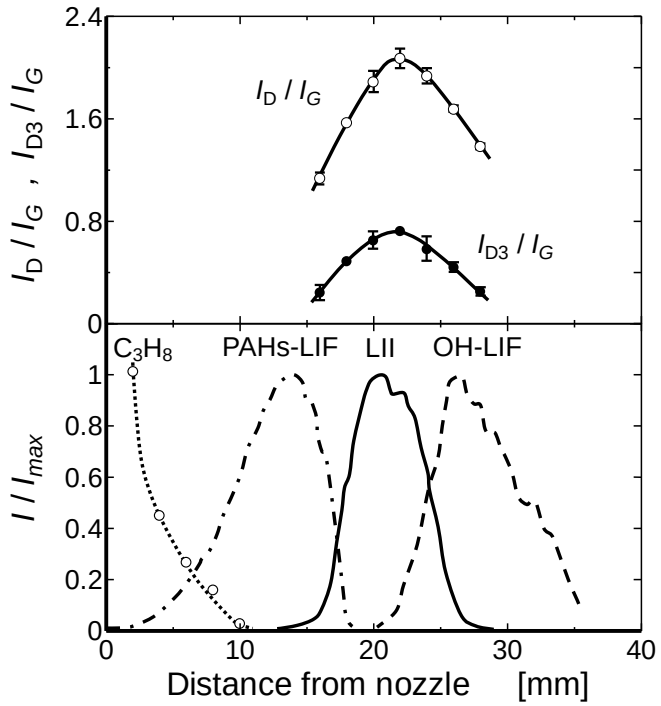
2.4
1.6
0.8
0
I_D / I_G , I_{D3} / I_G
I_D / I_G
I_{D3} / I_G
C_3H_8
PAHs-LIF
LII
OH-LIF
1
0.8
0.6
0.4
0.2
0
I / I_{max}
0
10
20
30
40
Distance from nozzle [mm]

Figure 5

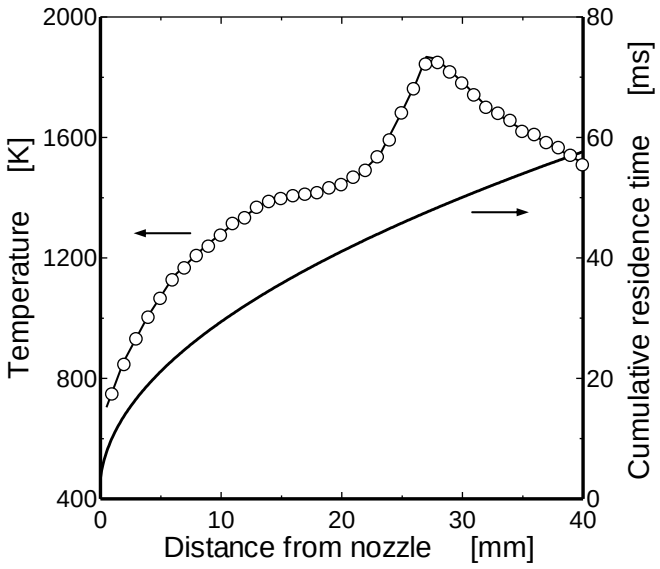
2000
1600
1200
800
400
Temperature [K]
80
60
40
20
0
Cumulative residence time [ms]
0
10
20
30
40
Distance from nozzle [mm]

Figure 6